ADVANCED MATERIALS
www.advmat.de

Gold-Template-Assisted Mechanical Exfoliation of Large-Area 2D Layers Enables Efficient and Precise Construction of Moiré Superlattices

Kang Wu, Hao Wang, Meng Yang, Li Liu, Zhenyu Sun, Guojing Hu, Yanpeng Song, Xin Han, Jiangang Guo, Kehui Wu, Baojie Feng, Chengmin Shen, Yuan Huang, Youguo Shi, Zhigang Cheng, Haitao Yang, Lihong Bao,* Sokrates T. Pantelides, and Hong-Jun Gao*

Moiré superlattices, consisting of rotationally aligned 2D atomically thin layers, provide a highly novel platform for the study of correlated quantum phenomena. However, reliable and efficient construction of moiré superlattices is challenging because of difficulties to accurately angle-align small exfoliated 2D layers and the need to shun wet-transfer processes. Here, efficient and precise construction of various moiré superlattices is demonstrated by picking up and stacking large-area 2D mono- or few-layer crystals with predetermined crystal axes, made possible by a gold-template-assisted mechanical exfoliation method. The exfoliated 2D layers are semiconductors, superconductors, or magnets and their high quality is confirmed by photoluminescence and Raman spectra and by electrical transport measurements of fabricated field-effect transistors and Hall devices. Twisted homobilayers with angle-twisting accuracy of ≈0.3°, twisted heterobilayers with sub-degree angle-alignment accuracy, and multilayer superlattices are precisely constructed and characterized by their moiré patterns, interlayer excitons, and second harmonic generation. The present study paves the way for exploring emergent phenomena in moiré superlattices.

1. Introduction

Moiré superlattices, formed by stacking 2D mono- or few-layer crystals at a specific twist angle, have emerged as novel correlated material systems due to their tailored band topology and electronic correlations induced by the periodic moiré potentials.[1–3] Tuning the twist-angle degree of freedom and the types of constituent 2D layers,[4] including graphene, transition metal dichalcogenides (TMDs), and beyond, enables the observation of exotic quantum phenomena, such as unconventional superconductivity,[5,6] correlated insulating states,[7,8] moiré excitons,[9–12] fractional quantum anomalous Hall states,[13] and interfacial ferroelectricity.[14,15] However, the construction of moiré superlattices faces reproducibility and efficiency issues[16,17] due to the small sizes (usually smaller than 40 μm) and the extremely low production yield of constituent 2D mono- or

K. Wu, H. Wang, M. Yang, L. Liu, Z. Sun, G. Hu, Y. Song, X. Han, J. Guo, K. Wu, B. Feng, C. Shen, Y. Shi, Z. Cheng, H. Yang, L. Bao, H.-J. Gao
Institute of Physics
Chinese Academy of Sciences
Beijing 100190, P. R. China
E-mail: htyang@iphy.ac.cn; lhbao@iphy.ac.cn

K. Wu, H. Wang, M. Yang, Z. Sun, K. Wu, B. Feng, C. Shen, Y. Shi, Z. Cheng, H. Yang, L. Bao, S. T. Pantelides, H.-J. Gao
School of Physical Sciences and CAS Key Laboratory of Vacuum Physics
University of Chinese Academy of Sciences
Beijing 100049, P. R. China

X. Han, Y. Shi
Center of Materials Science and Optoelectronics Engineering
University of Chinese Academy of Science
Beijing 100049, P. R. China

Y. Huang
Advanced Research Institute of Multidisciplinary Science
Beijing Institute of Technology
Beijing 100081, P. R. China

Y. Shi, Z. Cheng
Songshan Lake Materials Laboratory
Dongguan, Guangdong 523808, P. R. China

H. Yang, L. Bao, H.-J. Gao
Hefei National Laboratory
Hefei, Anhui 230088, P. R. China

S. T. Pantelides
Department of Physics and Astronomy & Department of Electrical and Computer Engineering
Vanderbilt University
Nashville, TN 37235, USA

The ORCID identification number(s) for the author(s) of this article can be found under https://doi.org/10.1002/adma.202313511

DOI: 10.1002/adma.202313511

few-layer crystals obtained by the conventional Scotch-tape exfoliation method.[18] A tear-and-stack method[19] has been developed to construct twisted homojunctions, in which a mono- or few-layer flake exfoliated by the Scotch-tape method is torn into two sections, and then one section is picked up and stacked onto the other section with a specific twist angle using dry-transfer techniques.[20] This method typically requires the exfoliated mono- and few-layer crystals to be isolated from thick crystals, as well as lateral dimensions larger than 30 μm, which is challenging for TMD exfoliation[13–15] and extremely difficult for exfoliation of air-sensitive materials. To construct twisted heterojunctions, two constituent atomically thin layers are angle-aligned through their straight edges[6,21,22] or their crystal axes as determined by polarization-resolved second harmonic generation (SHG).[9–12] However, the straight edges are typically used for aligning graphene/hBN heterostructures,[6,21,22] but rarely used for aligning twisted TMD heterobilayers due to uncertainties of zigzag directions of exfoliated monolayer TMDs inferred by the straight edges considering their small sizes. Polarization-resolved SHG measurements before alignment complicate the fabrication process and are not applicable to determine the crystal axes of air-sensitive or centrosymmetric crystals.

To overcome the issue of small sizes of exfoliated crystals by the Scotch-tape method, a gold-assisted exfoliation method[23,24] has been developed to obtain large, 2D monolayers. The method has universal applicability to a wide variety of 2D materials.[23] However, due to the strong interaction between a gold film and 2D crystals, a wet-transfer process (wet-etching of the underlying gold film) is entailed when attempting to transfer the exfoliated 2D crystals. The prerequisite for constructing high-quality moiré superlattices is the ability to dry-transfer the exfoliated 2D crystals. Degradation and contamination arising from wet-transfer hinder the observation of correlated quantum phenomena from moiré superlattices. Therefore, the gold-assisted exfoliation method is excluded from constructing high-quality moiré superlattices. Other exfoliation methods have been developed, including gold-tape exfoliation,[25] Al_2O_3-assisted exfoliation,[26] vacuum exfoliation,[27,28] suspended-material exfoliation,[29] and gold-mesh tape exfoliation.[30] These methods encounter problems in fabricating moiré superlattices, such as difficulties in detaching exfoliated 2D layers from substrates,[26–29] the need for a wet-transfer process[25] to fabricate heterostructures, small sizes of exfoliated 2D layers,[26,29,30] and narrow applicability to specific types of 2D crystals.[25,26,28,30] Therefore, to construct moiré superlattices efficiently and precisely, it is critical to develop a universal, efficient, and dry-transfer-compatible mechanical exfoliation method for obtaining large-area and high-quality constituent 2D layers.

In this paper, we report the efficient and precise construction of moiré superlattices enabled by a novel gold-template-assisted (Au-template-assisted) mechanical exfoliation method. Using this approach on pre-fabricated Au-patterned SiO_2 substrates, a wide variety of 2D atomically thin crystals, including TMDs, superconductors, and magnets, are successfully exfoliated. The exfoliated mono- and few-layer crystals in direct contact with exposed rectangular SiO_2 reach a dimension of 40 μm with high production yield. We have conducted Raman, photoluminescence (PL), and SHG characterizations of the exfoliated 2D TMD layers (WS_2, MoS_2, WSe_2, and $MoSe_2$) to confirm their quality, uniformity, and surface cleanness. Moreover, these optical signals of TMD layers on exposed rectangular SiO_2 substrates are significantly stronger than those on Au films. This indicates the apparent advantages of our Au-template-assisted exfoliation method in studying the intrinsic optical properties of atomically thin 2D layers compared to the conventional Au-assisted exfoliation method.[24] Furthermore, we have successfully fabricated field-effect-transistor (FET) devices and Hall devices by picking up exfoliated bi- to few-layer BP and $NbSe_2$. These results demonstrate that our Au-template-assisted mechanical method is compatible with dry-transfer techniques and has broad applicability in studying layer-dependent electrical transport properties of 2D materials. The high yield of uniform and clean, large-area 2D crystals using our exfoliation method enables the construction of high-quality moiré superlattices with excellent reproducibility, high efficiency, and precise custom twist angles. By picking up and stacking either two adjacent flakes or different flakes aligned through their adjacent long straight steps across layers, twisted homojunctions with angle-twisting accuracy of ≈0.3° or heterojunctions with sub-degree angle-alignment accuracy are obtained. These moiré superlattices are further characterized by visualization of moiré patterns, polarization-resolved SHG, interlayer excitons (ILXs), and SHG spectra. The present work paves the way for exploring emergent phenomena in moiré superlattices and can accelerate the development of twistronics.

2. Results and Discussion

2.1. Au-Template-Assisted Mechanical Exfoliation Method

The Au-template-assisted mechanical exfoliation approach that we introduced to facilitate the construction of moiré superlattices is illustrated in **Figure 1a**. The Au-patterned SiO_2 substrates are fabricated using the standard photolithography and bilayer resist lift-off techniques (see Experimental Section for details). The surface of the Au-patterned SiO_2 substrate is divided into two types of regions: one consists of isolated rectangles of exposed SiO_2, while the other is covered by a thin layer of continuous Au film (≈10 nm). To simplify the description, we refer to the two types of regions as the rectangular SiO_2 surface and the Au film in the following text, respectively. Prior to exfoliation, it is necessary to perform an argon (Ar) plasma etching process for surface cleaning of Au-patterned SiO_2 substrates (see Experimental Section for details).

To demonstrate the feasibility of the Au-template-assisted mechanical exfoliation method, we chose MoS_2 as a representative crystal to carry out the exfoliation process. As shown in Figure 1b,c, large-area monolayer (1L), bilayer (2L), and trilayer (3L) MoS_2 on rectangular SiO_2 surfaces are successfully obtained. The isolated atomically thin layers on rectangular SiO_2 surfaces have lateral sizes of 30 μm × 40 μm. The maximum size of continuous atomically thin layers achievable on the Au-patterned SiO_2 substrates using the Au-template-assisted exfoliation method reaches a millimeter scale, which is comparable with the maximum size achievable on the Au-film substrates using the Au-assisted exfoliation method[23] (Figure S1, Supporting Information). In Figure S1c (Supporting Information), it can be seen that the macroscopic size of exfoliated 2D layers is almost the same as the size of the bulk crystals for both methods. Due

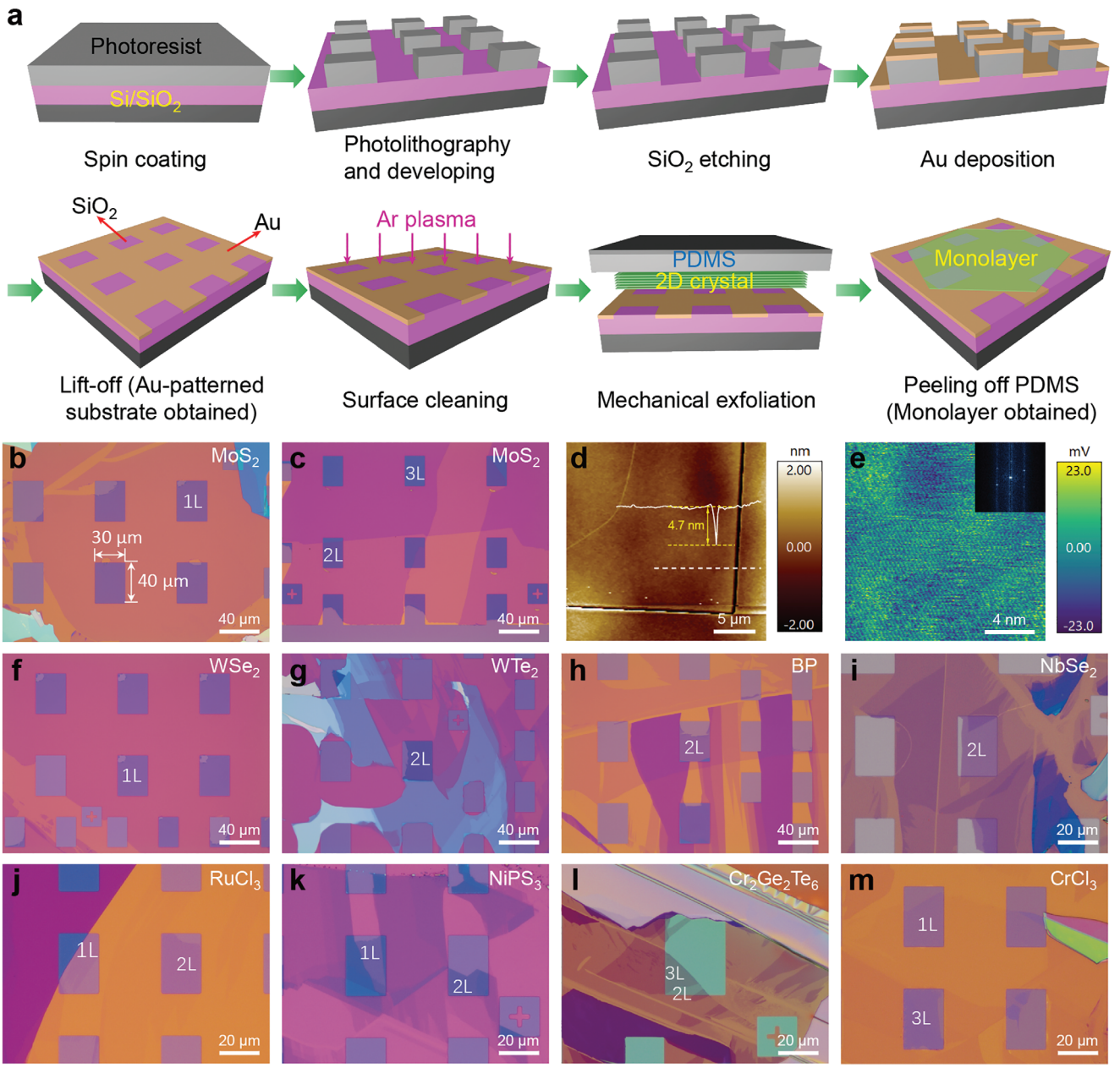

Figure 1. Au-template-assisted mechanical exfoliation of large-area 2D atomically thin layers. a) Schematic depiction of the Au-template-assisted mechanical exfoliation method, including fabrication of Au-patterned SiO_2 substrates (spin coating of photoresist, photolithography, developing, SiO_2 etching, Au deposition, lift-off), surface cleaning by argon plasma, and mechanical exfoliation. Finally, large-area 2D atomically thin layers are obtained on Au-patterned SiO_2 substrates. b) Optical image of exfoliated large-area monolayer (1L) MoS_2. c) Optical images of exfoliated large-area bilayer (2L), and trilayer (3L) MoS_2. The sizes of the isolated atomically thin layers on rectangular SiO_2 surfaces reach dimensions of 30 μm × 40 μm. d) AFM image of exfoliated monolayer MoS_2 near the boundary of rectangular SiO_2 substrate and the surrounding Au film. e) Atomically resolved LFM image of monolayer MoS_2 on rectangular SiO_2 substrate. The perfect-crystal lattice and clear diffraction pattern indicate the cleanness and high quality of exfoliated-monolayer MoS_2. f–m) Optical images of exfoliated typical large-area 2D atomically thin layers, including semiconductors (WSe_2, WTe_2, black phosphorus), superconductor ($NbSe_2$), quantum spin liquid ($RuCl_3$), ferromagnets ($NiPS_3$, $Cr_2Ge_2Te_6$), and antiferromagnet ($CrCl_3$).

to the presence of some cracks (Figure S1a,b, Supporting Information), the maximum size of continuous atomically thin layers achievable is usually smaller than the macroscopic size of exfoliated 2D layers. Compared with the conventional Scotch-tape exfoliation on normal SiO_2 substrates, the lateral sizes of exfoliated 2D layers and the production yield are greatly improved by our Au-template-assisted exfoliation (Figure S2a,b, Supporting Information) on Au-patterned SiO_2 substrates. We also fabricated Au-patterned SiO_2 substrates with patterns of different shapes and sizes, including rectangles with sizes of 15 × 20 μm^2, rectangles with sizes of 20 × 30 μm^2, rectangles with sizes of 30 × 40 μm^2, circles with a diameter of 32 μm, and ribbons with a

width of 20 μm (Figure S2c–g, Supporting Information). Furthermore, when the distance between adjacent rectangles is reduced from 60 μm (Figure S2d, Supporting Information) to less than 10 μm (Figure S2h, Supporting Information), the area ratio of exposed SiO_2 over the entire Au-patterned substrate increases from ≈10% to ≈60%. The exfoliation results and the thickness uniformity for each SiO_2 rectangle remain unaffected. As the exfoliation yield is directly proportional to the total number of SiO_2 rectangles within a specific region with a constant area, the exfoliation yield is increased when reducing the distance between adjacent SiO_2 rectangles. Considering both the exfoliation yield and the large areas of 2D layers, rectangles with sizes of 30×40 μm^2 are the most preferred patterns for exfoliation, with the distance between each rectangle reduced to less than 10 μm.

We tried to enlarge the sizes of the SiO_2 rectangles and investigate the influence of feature sizes on the exfoliation yield of MoS_2 (Figure S3, Supporting Information). The exfoliation yield gradually decreases from ≈60% to ≈6% as the sizes of the SiO_2 rectangles increase from 30×40 to 60×80 μm^2. Upon further enlargement to 80×120 μm^2, although the exfoliation yield drops significantly to ≈0.1%, it is still possible to find SiO_2 rectangles covered by monolayer MoS_2. The feasibility of our Au-template-assisted mechanical exfoliation method relies on two key points. First, the continuous Au film provides sufficient adhesion force between 2D crystals and the Au-patterned SiO_2 substrates.[23,24] Second, the relatively smooth transition at the boundary of rectangular SiO_2 substrate and surrounding Au film ensures the continuous exfoliation of mono- to few-layer crystals. Figure 1d shows an AFM image of a monolayer MoS_2 sample and a height profile across the boundary of the rectangular SiO_2 substrate and surrounding Au film. The height profile indeed presents a relatively smooth transition, except for the presence of nanoscale hollows (≈4.7 nm) or sub-nanometer steps at the boundary, which are unavoidable during the fabrication process of Au-patterned SiO_2 substrates. Figure 1e and the inset are an atomic-resolution image of the monolayer MoS_2 sample on a rectangular SiO_2 substrate and its corresponding fast Fourier transformation (FFT) result. A clear crystal lattice is observed, indicating the cleanness of the exfoliated monolayer MoS_2.

Beyond MoS_2, a variety of atomically thin large-area 2D crystals from monolayer to few-layer can be obtained using our Au-template-assisted mechanical exfoliation method. The exfoliated 2D crystals include semiconductors (WSe_2, WTe_2, black phosphorus), superconductor ($NbSe_2$), quantum spin liquid ($RuCl_3$), ferromagnets ($NiPS_3$, $Cr_2Ge_2Te_6$), antiferromagnet ($CrCl_3$), and others (Figure 1f–m; Figure S4, Supporting Information), demonstrating the universality of our Au-template-assisted mechanical exfoliation method. It is worth noting that for certain crystals, such as BP, $PtSe_2$, and FeSe, obtaining monolayer samples on a SiO_2 surface using our Au-template-assisted exfoliation method remains challenging due to the insufficient adhesion force between those monolayers and the Au-patterned SiO_2 substrates. Optimizing the Au-patterned SiO_2 substrate to achieve a completely smooth transition at the boundaries of rectangular SiO_2 and its surrounding Au films may be a feasible approach to increase the exfoliation yield of those monolayers. Similar to the Au-assisted exfoliation method,[23,24] the exfoliated 2D atomically thin layers on Au-patterned SiO2 substrates exhibit continuous changes in layer thickness with clear optical contrasts,[31,32] making it convenient to determine the corresponding layer number of mono- or few-layer crystals (Figure S5d,h, Supporting Information). The layer numbers of exfoliated 2D layers on rectangular SiO2 substrates are further confirmed by the following optical characterizations.

2.2. Raman and PL Spectra of Exfoliated 2D Atomically Thin Layers

In 2D atomically thin crystals, Raman and PL spectroscopies are highly sensitive to strains, defects, and doping, and, therefore, they are widely used as indicators of crystal quality.[25,29,33] **Figure 2**a–d shows Raman spectra of exfoliated monolayer and bilayer TMDs (WS_2, MoS_2, WSe_2, and $MoSe_2$) on rectangular SiO_2 substrates and monolayer TMDs on Au films, for which the Raman intensity is multiplied by a factor of 10. Notably, for monolayer and bilayer TMDs on rectangular SiO_2 substrates, all the dominant Raman peaks have symmetric lineshapes and high signal-to-noise ratios. However, due to the strong binding energy[23] and strains[34] between 2D layers and Au film, the Raman-peak intensity of monolayer TMDs on Au films is significantly reduced, with a lower signal-to-noise ratio, while the second-order phonon vibration modes (marked by asterisks in Figure 2a–c) are barely visible. We also measured Raman spectra of other 2D atomically thin layers, such as $NbSe_2$, black phosphorus (BP), and $Cr_2Ge_2Te_6$, and discussed their layer-dependent Raman characteristics in Figure S6 (Supporting Information).

Figure 2e–h shows the PL spectra of monolayer and bilayer TMDs on rectangular SiO_2 substrates and monolayer TMDs on Au films, for which the PL intensity is multiplied by a factor of 100. The PL signals are essentially completely quenched for monolayer TMDs on Au films, which is attributed to the strong charge transfer at the interface.[24,27,35] In contrast, all monolayer TMDs on exposed rectangular SiO_2 substrates present a narrow full-width at half-maximum (FWHM) of ≈38 meV at 1.93 eV (WS_2, Figure 2e), ≈53 meV at 1.82 eV (MoS_2, Figure 2f), ≈53 meV at 1.61 eV (WSe_2, Figure 2g), and ≈52 meV at 1.53 eV ($MoSe_2$, Figure 2h), respectively. All of these FWHM values are comparable to or smaller than the previously reported FWHM values of monolayer TMDs obtained by either the conventional Scotch-tape exfoliation method or the CVD growth method (Table S1, Supporting Information). The narrow FWHM of the PL peaks indicates the high quality of our exfoliated monolayer TMDs.

Furthermore, Raman, PL, and SHG intensity mappings are conducted to confirm the uniformity of exfoliated monolayer TMDs. Figure 2i shows an optical image of an exfoliated monolayer MoS_2 sample on the Au-patterned SiO_2 substrate. Both the Raman intensity mapping of the $E1\ 2\ g$ mode (≈382 cm^{-1}, Figure 2j) and the PL intensity mapping of the A exciton (≈1.82 eV, Figure 2k) of exfoliated monolayer MoS_2 samples on rectangular SiO_2 substrates are very uniform, indicating their high quality and uniformity. The distinct intensity contrasts between monolayer TMDs on exposed rectangular SiO_2 substrates and monolayer TMDs on Au films suggest that SiO_2 substrates are more favorable for studying the intrinsic optical properties of 2D crystals. This is further confirmed by the SHG intensity mapping on monolayer WS_2 (Figure 2l). Slight inhomogeneity

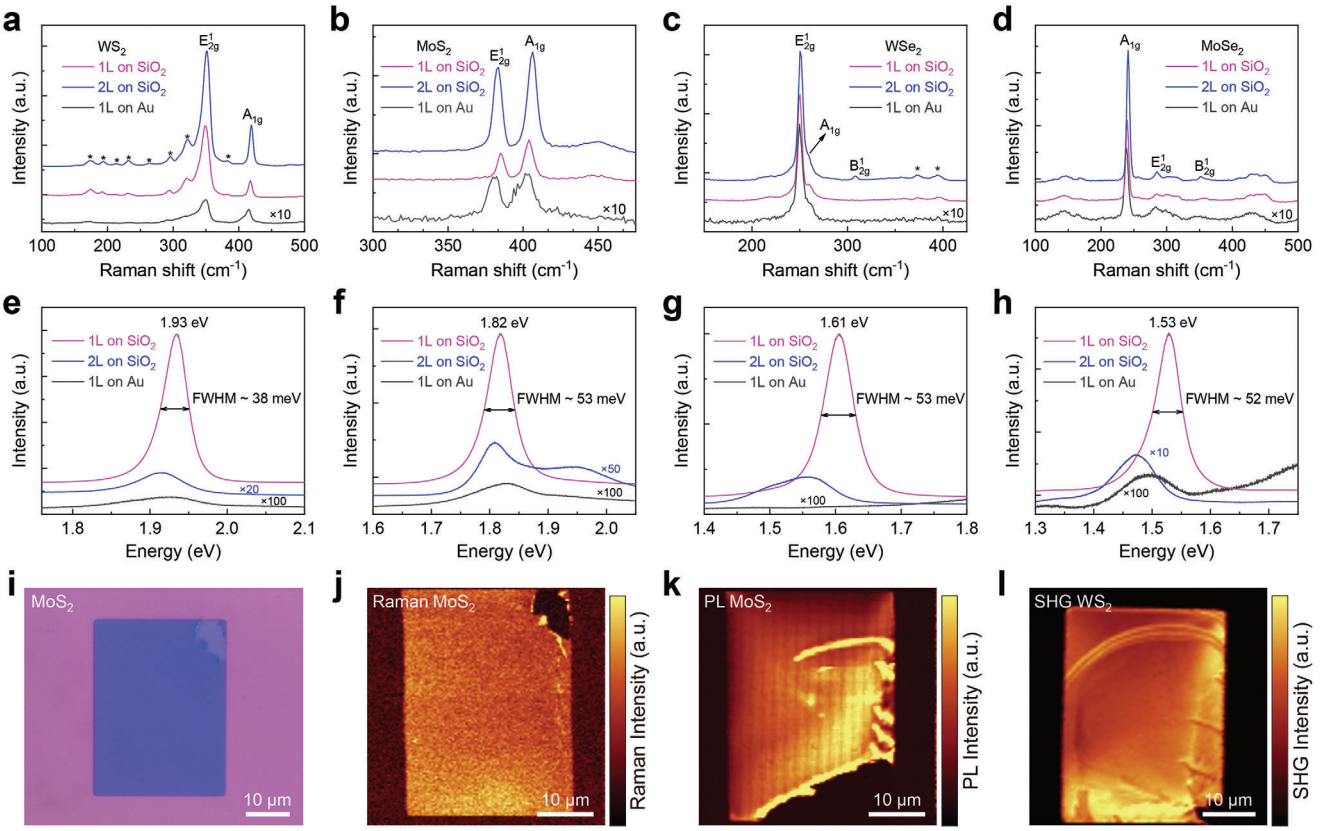

Figure 2. Raman spectra and PL spectra of TMD layers (WS_2, MoS_2, WSe_2, $MoSe_2$) obtained by the Au-template-assisted exfoliation method. a–d) Raman spectra of monolayer and bilayer TMDs on both rectangular SiO_2 substrates and monolayer TMDs on Au films at room temperature. Due to the strong interaction of 2D materials with Au films, the Raman intensity of monolayer TMDs on Au films is greatly suppressed. e–h) PL spectra of monolayer and bilayer TMDs on rectangular SiO_2 substrates and monolayer TMDs on Au films at room temperature. The normalized PL intensity of monolayer TMDs on rectangular SiO_2 substrates is stronger than that on Au films. The small FWHM of monolayer WS_2 (≈37 meV), MoS_2 (≈53 meV), WSe_2 (≈53 meV), and $MoSe_2$ (≈52 meV) reveals the high quality of exfoliated TMD layers. i) Optical image of an exfoliated monolayer MoS_2. j) Raman mapping image of the monolayer MoS_2 in (i). k) PL mapping image of a monolayer MoS_2. l) SHG mapping image of a monolayer WS_2. The Raman, PL, and SHG mapping images indicate the monolayer nature and uniformity of exfoliated layers on the rectangular SiO_2 substrates. The distinct mapping intensity contrasts between monolayer TMDs on exposed rectangular SiO_2 substrates and monolayer TMDs on Au films suggest that monolayer TMDs on SiO_2 substrates are more favorable for studying the intrinsic optical properties of 2D crystals.

of strain distribution is observed at the rectangular edges due to the high sensitivity of optical signals to strain variations.[25,29] Occasionally, minor wrinkles and holes are observed in one corner of the rectangular SiO_2 substrates, as seen in Figure 2i–l. These effects arise from the bursting of monolayer-capped bubbles, which are unavoidably formed in one corner of the rectangular SiO_2 substrates when 2D crystals on polydimethylsiloxane (PDMS) are contacted with Au-patterned substrates.

2.3. Layer-Dependent Electrical Transport Properties of BP and $NbSe_2$

Gold-film substrates are not suitable for studying the intrinsic electronic properties of 2D materials due to the charge doping effect of gold films on 2D materials.[36] Dry-transfer techniques are widely used in studies of intrinsic electrical transport properties of exfoliated 2D atomically thin crystals. Through dry-transfer techniques, high-quality encapsulated structures or clean dielectric interfaces are achieved,[37–39] and arbitrarily designed charge transfer doping is possible by transferring cleanly exfoliated 2D materials onto functionalized substrates.[40,41] The direct exfoliation of mono- to few-layer 2D atomically thin crystals on exposed rectangular SiO_2 substrates by our Au-template-assisted exfoliation method eliminates the gold-doping effect and significantly facilitates the dry pick-up of mono- to few-layer 2D atomically thin crystals. We choose three typical 2D atomically thin crystals (BP, $NbSe_2$, and MoS_2) to fabricate field-effect transistors or Hall devices by dry-transfer techniques for studying their layer-dependent electrical transport properties. Due to the degradation of few-layer BP and $NbSe_2$ in air, the study of the electrical transport properties of these materials is quite challenging, requiring additional protection or encapsulation.[39,42] This issue is circumvented during our device fabrication process, which is carried out on a motorized transfer stage inside a glovebox (see Experimental Section). Figure S7 (Supporting Information) shows optical images taken during different fabrication steps of a representative top-gated bilayer BP FET to illustrate the compatibility of our Au-template-assisted exfoliation method with dry-transfer techniques.

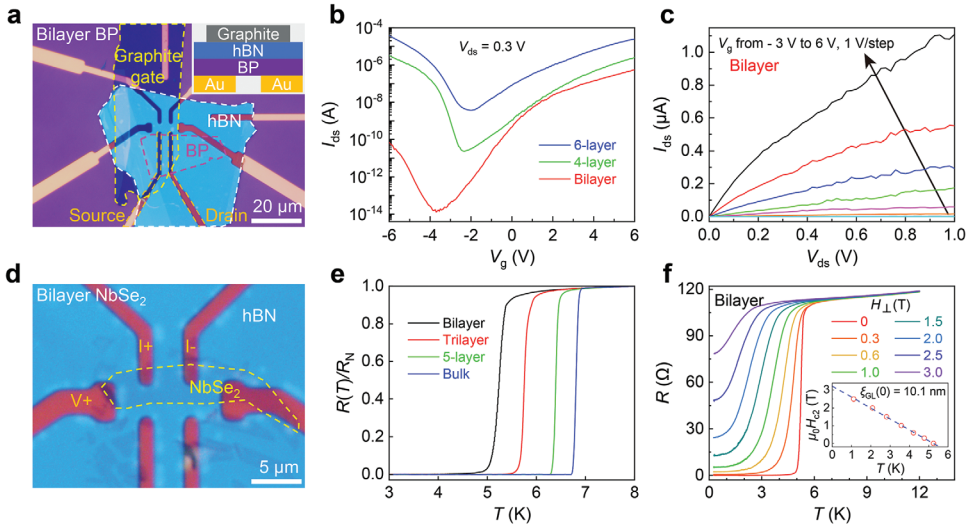

Figure 3. Layer-dependent electrical transport properties of 2D atomically thin BP and $NbSe_2$. a) Optical image of a top-gated bilayer BP FET with pre-patterned Cr/Au (3 nm/18 nm) contact electrodes and transferred graphite serving as the gate electrode. Inset: schematic of the top-gated BP FET. b) Transfer characteristics of BP FETs with varying channel thickness (bilayer, four-layer, and six-layer) at $V_{ds} = 0.3$ V in logarithmic scale. The bilayer device exhibits n-type dominated transport behavior and a high on/off ratio of more than 10^7. Both the four-layer and six-layer devices show ambipolar transport behavior with comparable on/off ratios on the hole doping and electron doping sides. c) Output characteristics of the top-gated bilayer BP FET in (a) at V_{ds} ranging from 0 to 1 V. The gate voltage V_g is from −3 to 6 V with a step of 1 V. d) Optical image of a bilayer $NbSe_2$ Hall device with pre-patterned Cr/Au (3 nm/18 nm) contact electrodes. e) Temperature-dependent resistance of $NbSe_2$ devices with varying thickness (bilayer, trilayer, five-layer, and bulk). As the thickness of $NbSe_2$ varies from bulk to bilayer, the $T_c(0.5R_N)$ decreases from 6.81 to 5.25 K. f) Temperature-dependent resistance of the bilayer $NbSe_2$ device in (d) under different out-of-plane magnetic fields. Inset: H_{c2}-T phase diagram defined by $R(H_{c2}, T) = 0.5R_N$.

Figure 3a shows an optical image of the bilayer BP FET with the corresponding schematic of the device structure shown in the inset. Transfer characteristics of top-gated BP FETs with varying thickness (bilayer, four-layer, and six-layer) at $V_{ds} = 0.3$ V in logarithmic scale are shown in Figure 3b. The bilayer device exhibits n-type dominated transport behavior and an on/off ratio of more than 10^7, which is superior to the previously reported bilayer BP FET.[39] Both the four-layer and six-layer devices show ambipolar transport behavior with comparable on/off ratios on the hole doping and electron doping sides. Figure 3c shows the output characteristics of the top-gated bilayer BP FET at V_{ds} ranging from 0 to 1 V and gate voltage V_g ranging from −3 to 6 V with a step of 1 V, from which a trend of current saturation is observed. More details about transport measurements of BP FETs are shown in Figure S8 (Supporting Information). In contrast, the thickness of BP layers used in reported field-effect transistors and Hall devices is usually larger than 3 nm (>five-layer),[39,43,44] while studies of thinner BP layers are limited to optical characterizations,[27,32,45] such as Raman, PL, reflection spectroscopy, and angle-resolved photoemission spectroscopy. Therefore, the successful electrical transport measurements of BP devices fabricated with thin BP samples down to the bilayer demonstrate the significant advantages of our Au-template-assisted mechanical exfoliation method in studying the electrical transport properties of atomically thin 2D crystals.

We have further investigated the layer-dependent superconducting properties of atomically thin $NbSe_2$ Hall devices. A typical optical image of a bilayer $NbSe_2$ Hall device with pre-patterned Cr/Au electrodes is shown in Figure 3d. Figure 3e shows the temperature dependence near the superconducting transition of the normalized resistance (R/R_n) for $NbSe_2$ Hall devices of varying thickness (bilayer, trilayer, five-layer, and bulk). R_n represents the normal-state resistance taken at $T = 8$ K. A bulk $NbSe_2$ Hall device was fabricated by the deterministic transfer method[20] with a referenced T_c of 6.81 K. Superconductivity is observed for all samples down to the bilayer thickness. As the thickness of $NbSe_2$ varies from five-layer to bilayer, the superconducting transition temperature (T_c, defined as the temperature at which $R = 0.5R_N$) decreases from 6.40 to 5.25 K, which is consistent with previous reports.[39,42,46] Additionally, the five-layer $NbSe_2$ Hall device shows a sharp superconducting transition with a ΔT of 0.17 K, while a broadening is observed for $NbSe_2$ Hall devices of trilayer thickness ($\Delta T = 0.57$ K) and bilayer thickness ($\Delta T = 1.82$ K). We also conducted temperature-dependent resistance measurements of the bilayer $NbSe_2$ device under different out-of-plane magnetic fields (Figure 3f) and plotted the H_{c2}-T phase diagram (the inset in Figure 3f). H_{c2} is the upper critical field defined by $R(H_{c2}, T) = 0.5R_N$. A linear relationship between H_{c2} and T is observed, which can be explained by the standard Ginzburg–Landau (GL) theory of 2D semiconductors, $H_{c2}(T) = \frac{\phi_0}{2\pi\xi_{GL}(0)^2}(1 - \frac{T}{T_c})$, where ϕ_0 is the magnetic flux quantum and $\xi_{GL}(0)$ is the in-plane GL coherence length at zero temperature. A linear fit between H_{c2} and T yields $\xi_{GL}(0) = 10.1$ nm, which is close to the bulk value and consistent with the previously reported value on bilayer $NbSe_2$.[46] More details about transport measurements of $NbSe_2$ Hall devices are shown in Figure S9 (Supporting Information). Comparisons of the layer-dependent T_c, $T_{c\text{-onset}}$, $T_{c\text{-zero}}$, ΔT, residual resistance ratio, $H_{c2}(0)$, and $\xi_{GL}(0)$ of few-layer $NbSe_2$ are shown in Table S2 (Supporting Information). The successful fabrication of atomically thin $NbSe_2$ Hall devices down to bilayer thickness further demonstrates the excellent compatibility of our Au-template-assisted mechanical

exfoliation method with dry-transfer techniques, which greatly facilitates the construction of van der Waals heterostructures. As for monolayer $NbSe_2$, while we can obtain it, the relatively small size of ≈10 μm (Figure S4h, Supporting Information) brings a challenge in fabricating high-quality encapsulated devices. Despite having devoted great efforts to directly fabricate a monolayer $NbSe_2$ Hall device on an exfoliation substrate, the extreme sensitivity of monolayer $NbSe_2$ hinders the observation of superconductivity (Figure S10, Supporting Information). We also fabricated top-gated monolayer, bilayer, and trilayer MoS2 FETs (Figure S11, Supporting Information), and confirmed the feasibility to directly fabricate devices on the Au-patterned SiO_2 substrates (Figure S12, Supporting Information).

2.4. Construction of Moiré Superlattices

Our Au-template-assisted mechanical exfoliation can produce large-area 2D atomically thin crystal arrays on rectangular SiO_2 substrates and is compatible with dry-transfer techniques, enabling the efficient and precise construction of various moiré superlattices, including twisted homobilayers, heterobilayers, and multilayer superlattices. First, we fabricated twisted MoS_2 homobilayers by picking up and stacking two adjacent monolayer MoS_2 layers on rectangular SiO_2 substrates (Figure S13a,b, Supporting Information) using a poly(propylene) carbonate (PPC) film-capped hemispherical PDMS mounted on a glass slide. **Figure 4a** shows an optical image of a typical ≈1° twisted MoS_2 homobilayer with color-coded areas supported by hBN/PPC/SiO_2 stack. A schematic is shown in the inset of Figure 4a. No obvious bubbles are observed in the AFM image (Figure 4b), demonstrating the clean interface and flat surface of the twisted homobilayer. These features are further confirmed by the measured root-mean-square (RMS) roughness of 205 pm. The height profile across the step shows the monolayer features of each MoS_2 layer (≈0.65 and ≈0.44 nm). It is noted that there are some challenges in picking up the exfoliated 2D layers to construct moiré superlattices. For example, the inappropriate hBN thickness can increase the likelihood of failure to pick up the hBN/2D-layers stack using PPC, and the formation of some cracks and wrinkles leads to the reduction in the lateral sizes of the uniform regions of the fabricated moiré superlattices to 10–20 μm (Figure S13c, Note S1, Supporting Information). To characterize the interface quality of the fabricated twisted MoS_2 homobilayers, we visualized their moiré patterns by piezoresponse force microscopy (PFM). Figure 4c,d shows lateral PFM amplitude images of ≈1° and ≈3° twisted MoS_2 homobilayers, respectively, revealing clear moiré patterns with periods of ≈22.0 and ≈6.1 nm, confirming the high-quality interfaces. For the ≈0.1° twisted MoS_2 homobilayer (Figure S13c, Supporting Information), due to the large period of the moiré pattern and significant atomic reconstruction, visualization of the moiré superlattice with such a small twist angle is rather challenging. The PFM amplitude images of the ≈0.1° twisted MoS_2 homobilayer show distorted moiré patterns (Figure S14, Supporting Information). Next, we discussed the angle-twisting accuracy of the fabricated twisted MoS_2 homobilayers. We visualized the moiré patterns of four twisted MoS_2 homobilayer samples with a targeted twist angle of 56° and targeted moiré period of 4.51 nm by PFM (Figure S15, Supporting Information) to precisely assess the angle-twisting accuracy. Clear moiré patterns (Figure S15a, Supporting Information) and corresponding FFT patterns with sixfold symmetry (Figure S15b, Supporting Information) were observed at eight randomly selected positions. By analyzing the FFT spots, we were able to measure reciprocal vectors along three directions (marked by red dashed lines), then moiré periods and twist angles with an error bar were extracted (see Note S2, Supporting Information for more details). The angle-twisting accuracy is defined by comparing the measured twist angle with the targeted twist angle (Figure S16, Supporting Information). The targeted twist angle is 56°, and the obtained twist angles are all within the range of 55.7–56.3°, indicating an angle-twisting accuracy of ≈0.3°.

Beyond the twisted MoS_2 homobilayers, we also fabricated twisted WS_2/WSe_2 heterobilayers by angle-aligning the straight steps across layers of exfoliated WS_2 and WSe_2, as shown in Figure S17b,d (Supporting Information). The multiple adjacent straight steps across WS_2 or WSe_2 layers (marked by magenta and white dashed lines) have lateral sizes of up to 100 μm and are either parallel or at a ≈60° angle to each other, indicating the high precision in determining the zigzag directions of WS_2 or WSe_2 layers by their straight steps across WS_2 or WSe_2 layers (marked by magenta and white dashed lines) have lateral sizes of up to 100 μm and are either parallel or at a ≈60° angle to each other, indicating the high precision in determining the zigzag directions of WS_2 or WSe_2 layers by their straight steps. The monolayer TMDs on rectangular SiO_2 substrates (marked by the black dashed circles) are adjacent to the straight steps and have the same crystal orientations with the determined zigzag directions. Therefore, we can easily and efficiently construct the twisted TMD heterobilayers by angle-aligning the adjacent straight steps of constituent TMDs layers (see Experimental Section, Figure S18, Supporting Information).

Figure 4e,f shows an optical image and an SHG mapping image of a twisted WS_2/WSe_2 heterobilayer (sample 1). The heterobilayer region shows enhanced SHG mapping intensity compared to their individual-monolayer region, indicating an R-stacking configuration. Figure 4g shows the polarization-resolved SHG signals of the twisted WS_2/WSe_2 heterobilayer (magenta symbol), the monolayer WSe_2 (green symbol), and the monolayer WS_2 (blue symbol). The polarization of the incident laser is controlled by a motorized half-wave plate in the setup for the polarization-resolved SHG measurements with a laboratory coordinate system (Figure S19, Supporting Information). The polarization-resolved SHG intensity varies as $I_{\perp}(\theta) \propto \sin^2[3(\theta-\theta_a)]$,[47,48] where $I_{\perp}$ is the perpendicular component of SHG intensity when configuring the pass plane of polarizer along the *y*-axis, θ is twice the rotation angle of the half-wave plate, and θ_a is the angle of the armchair direction relative to the *x*-axis (see Experimental Section for more details about the configuration of SHG measurements). More twisted WS_2/WSe_2 heterobilayers (samples 2–4) and their corresponding SHG mappings and polarization-resolved SHG intensities are shown in Figure S20 (Supporting Information). We fitted the polarization-resolved SHG signals and extracted the armchair-direction angle θ_a with an error bar, as shown in Figure 4h. The error bar represents the uncertainty δ of the armchair direction determination, which is 0.2–0.3°. The twist angle of the WS_2/WSe_2 heterobilayer is $\Phi = |\theta_a(WS_2) - \theta_a(WSe_2)|$ with an accuracy Δ of $\approx 2\delta$, where

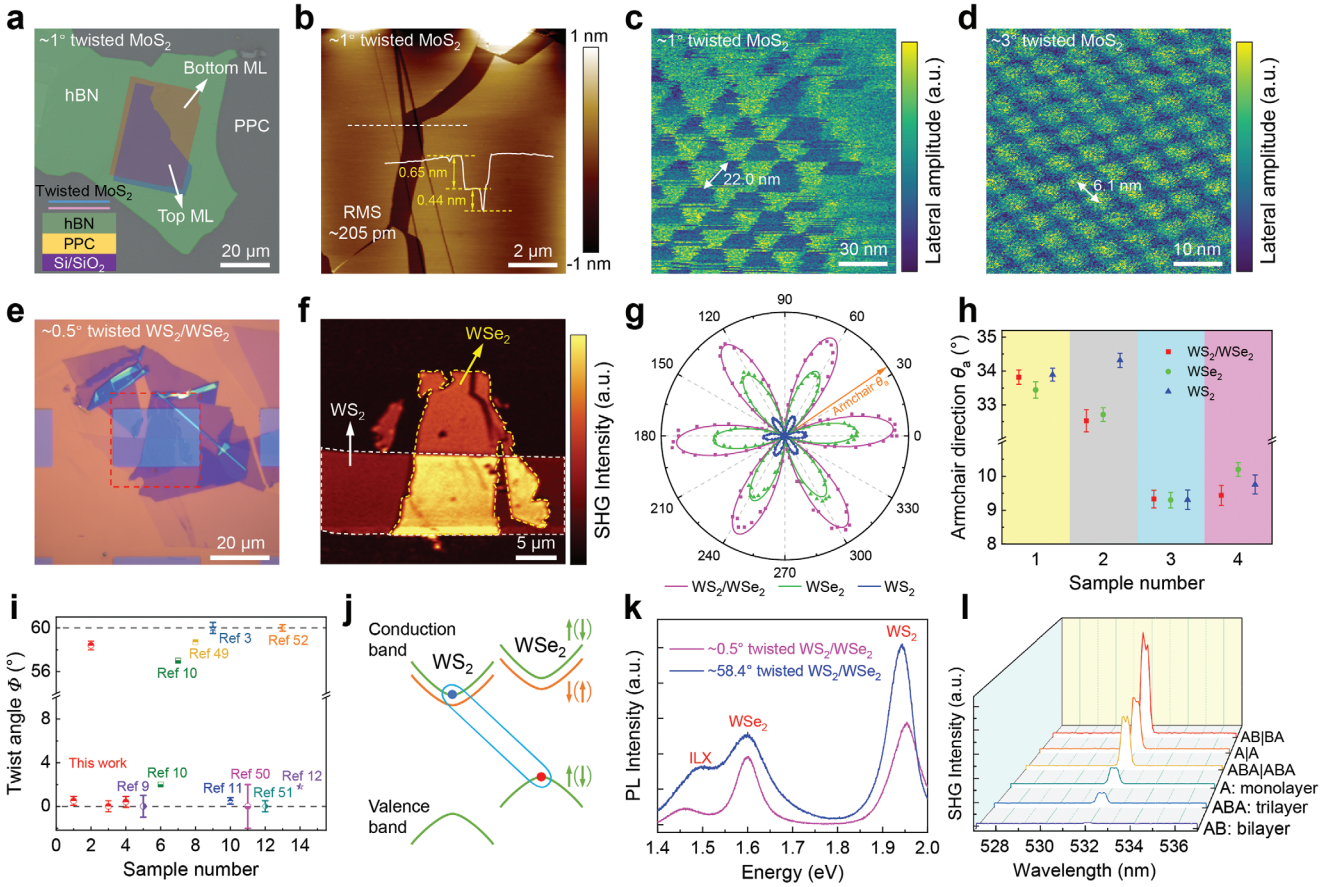

Figure 4. AFM, SHG, and interlayer exciton characterizations of twisted homobilayers, heterobilayers, and multilayer superlattices. a) Optical image of a ≈1° twisted MoS_2 homobilayer on hBN with color-coded areas representing hBN (green), bottom monolayer MoS_2 (orange), top monolayer MoS_2 (blue), and the overlapping region (violet) respectively. Inset: schematic structure of the fabricated twisted MoS_2 homobilayer. b) AFM image and height profile of the ≈1° twisted MoS_2 homobilayer in (a). No obvious bubbles are observed along with the measured RMS roughness of ≈205 pm, demonstrating the high-quality interface and clean surface of the twisted sample. The height profile across the step shows the monolayer features of each MoS_2 layer (≈0.65 nm, ≈0.44 nm). c,d) Lateral PFM images of ≈1° and ≈3° twisted MoS_2 homobilayers with evident moiré patterns. e) Optical image of a ≈0.5° twisted WS_2/WSe_2 heterobilayer (sample 1, R-stacking) on SiO_2 substrate with a thin hBN capping layer. f) SHG mapping of the area marked by the red dashed square in (e), which demonstrates the enhanced SHG signal at the overlapping (heterobilayer) region for an R-stacking heterobilayer. g) Polarization-resolved SHG signals and the corresponding fittings of the twisted WS_2/WSe_2 heterobilayer (magenta symbol), the constituent monolayer WSe_2 (green symbol), and the constituent monolayer WS_2 (blue symbol). h) The armchair directions of monolayer WS_2, monolayer WSe_2, and overlapped WS_2/WSe_2 heterolayer (samples 1–4) derived from the sixfold fittings of the polarization-resolved SHG signals. i) Comparison of the twist angle distribution with reported twisted TMD heterobilayers. j) Schematic of the type II band alignment of the WS_2/WSe_2 heterobilayer displays the formation of interlayer excitons. k) PL spectra of ≈0.5° (sample 1) and ≈58.4° (sample 2) twisted WS_2/WSe_2 heterobilayers at room temperature. The peaks at ≈1.46 eV (sample 1, R-stacking) and ≈1.50 eV (sample 2, H-stacking) indicate the existence of ILXs. l) 1SHG spectra of monolayer, bilayer, trilayer, twisted bilayer (A|A), twisted four-layer (AB|BA), twisted six-layer (ABA|ABA) MoS_2 superlattices. The twisted angles are 0° (A|A), 60° (AB|BA), and 0° (ABA|ABA) respectively. The SHG signal of the twisted four-layer MoS_2 superlattice is remarkably enhanced.

$\theta_a(WS_2)$ and $\theta_a(WSe_2)$ are the fitted armchair-direction angles of WS_2 and WSe_2, respectively. The angle-alignment accuracy of twisted TMD heterobilayers is defined as the difference between targeted and obtained twist angles. Then we compared the angle-alignment accuracy of samples prepared by different alignment methods, as shown in Figure 4i and **Table 1**. Previously, fabrication of twisted TMD heterobilayers by stacking individual layers either with the all-dry viscoelastic stamping method[9,10,20,49] or with the dry pick-up method[3,11,50–52] relied on polarization-resolved SHG to predetermine the crystal axes before the alignment, which complicates the fabrication process and reduces the efficiency. For comparison, the angle-alignment accuracy of our present method to fabricate twisted TMD heterobilayers by simply angle-aligning the straight steps across layers is below 1°, which is comparable or smaller than that of the above methods. Furthermore, our method can extend to centrosymmetric, multilayer, and air-sensitive materials due to the simplicity to get large-area 2D crystals with reliable straight steps on Au film.

As schematically shown in Figure 4j, when stacking monolayer WS_2 and WSe_2 to form twisted heterobilayers, type-II energy band alignment is built and interlayer excitons in which electrons and holes reside in WS_2 and WSe_2, respectively, are present. To reveal the features of the interlayer excitons, we measured the PL spectra of twisted WS_2/WSe_2 heterobilayers with both R-stacking (sample 1, ≈0.5°) and H-stacking (sample 2, ≈58.4°) configurations at room temperature, as shown in Figure 4k. The

Table 1. Comparison of angle-alignment accuracy of twisted TMD heterobilayers fabricated by different alignment methods. Note that the estimation of angle-alignment accuracy may differ from each other. In cases where reports mention the angle-alignment accuracy without specifying the twist angle, we use (0°) or (60°).

Sample number	Twisted TMDs	Targeted twist angle Φ_T [°]	Obtained twist angle $\Phi \pm \Delta$ [°]	Twist angle determination accuracy Δ [°]	Angle-alignment accuracy $\lvert\Phi_T-\Phi\rvert$ [°]	Alignment methods	Ref
1	WS_2/WSe_2	0	0.5 ± 0.4	≤0.5	0.5 ± 0.4	Angle-align the adjacent straight steps across crystal layers	This work
2		60	58.4 ± 0.4		1.6 ± 0.4		
3		0	0 ± 0.5		0 ± 0.5		
4		0	0.4 ± 0.5		0.4 ± 0.5		
5	$MoSe_2/WSe_2$	(0)	(0)	—	(0) ± 1	Angle-align the predetermined crystal axes using polarization-resolved SHG by the all-dry viscoelastic stamping method	[9]
6	$MoSe_2/WSe_2$	0	≈2	—	≈2.0		[10]
7	$MoSe_2/WSe_2$	60	≈57	—	≈3.0		[10]
8	MoS_2/WSe_2	60	≈58.7	—	≈1.3		[49]
9	$MoTe_2/WSe_2$	(60)	(60)	—	(0) ± 0.5	Angle-align the predetermined crystal axes using polarization-resolved SHG by the dry pick-up method	[3]
10	WS_2/WSe_2	0	≈0.5	0.3	0.5 ± 0.3		[11]
11	$MoSe_2/WSe_2$	(0)	(0)	—	(0) ± 2.0		[50]
12	WS_2/WSe_2	(0)	(0)	—	(0) ± 0.5		[51]
13	WS_2/WSe_2	60	60 ± 0.3	0.3	0 ± 0.3		[52]
14	$MoSe_2/WS_2$	0	≈1.8	—	≈1.8	Angle-align the straight edges of crystal flakes	[12]

PL peaks located at ≈1.61 and ≈1.93 eV are intralayer-exciton peaks of the WSe_2 and WS_2 monolayers, respectively. The PL peaks at ≈1.46 and ≈1.50 eV reveal the formation of interlayer excitons in both ≈0.5°and ≈58.4° twisted WS_2/WSe_2 heterobilayers, which is guaranteed by the high quality of our fabricated twisted heterobilayer samples. Note that the specific shape and intensity of interlayer exciton peaks vary from location to location on the twisted heterobilayer region (Figure S21, Supporting Information), which is common and consistent with previous reports.[9,10,25]

The capability of our Au-template-assisted mechanical exfoliation method to produce large-area 2D crystal arrays enables the construction of twisted multilayer homojunctions by arbitrarily stacking adjacent 2D layers with different thicknesses. For example, it is highly convenient to fabricate ≈0° twisted bilayer (A|A), ≈60° twisted four-layer (AB|BA), and ≈0° twisted six-layer (ABA|ABA) MoS_2 superlattices (Figure S22, Supporting Information). The SHG spectra of these twisted multilayer-MoS_2 homojunctions exhibit an increased signal intensity compared to their constituent monolayer, bilayer, and trilayer MoS_2 counterparts (Figure 4l), due to the broken inversion symmetry of the fabricated twisted homojunctions. Notably, the SHG signal intensity of the twisted four-layer MoS_2 is remarkably enhanced, being approximately six times that of monolayer MoS_2 and two times that of both the twisted bilayer and six-layer MoS_2 homojunctions.

3. Conclusion

In summary, we have developed a gold-template-assisted mechanical exfoliation method that is compatible with dry-transfer techniques and facilitates the construction of moiré superlattices with high efficiency, precision, and reproducibility. Our exfoliation method provides a universal and simple approach to obtain large-area 2D atomically thin layers of high quality, uniformity, and cleanness and can be used to study intrinsic optical properties and layer-dependent transport properties of various crystals, such as TMDs, superconductors, magnets, and air-sensitive materials. Moiré patterns, interlayer excitons, SHG imaging, and polarization-resolved SHG are performed to characterize our constructed moiré superlattices: twisted MoS_2 homobilayers, twisted WS_2/WSe_2 heterobilayers, and twisted multilayer-MoS_2 homojunctions. For twisted homojunctions, the angle-twisting accuracy is ≈0.3° achieved by picking up two adjacent 2D monolayers. For twisted heterobilayers, the angle-alignment accuracy achieved by angle-aligning the straight steps of two individual constituent 2D monolayers is sub-degree. The present work opens avenues for designing a wide range of novel moiré superlattices and exploring emergent phenomena based on new moiré systems.

4. Experimental Section

Fabrication of Au-Patterned SiO_2 Substrates: An SPR220-LOR bilayer resist lift-off process was used to fabricate Au-patterned SiO_2 substrates by photolithography. LOR 5A resist was spin-coated at 4000 r min^{-1}, and SPR220 3.0 was spin-coated at 5000 r min^{-1} on pre-cleaned Si/SiO_2 (285 nm) substrates, followed by baking at 180 °C for 5 min and 110 °C for 90 s, respectively. Then, a photolithography process was conducted using the Heidelberg DWL 66+ laser writing system. After developing the bilayer resist by AZ 300MIF developer and deionized water, reactive ion etching (RIE) with CHF_3/Ar as the etching gas was used to etch the exposed SiO_2 to a depth of 12 nm, with the patterned photoresist serving as a mask. Subsequently, Cr/Au (2 nm/13 nm) was deposited using an electron beam evaporation (EBD) system. At last, the remaining photoresists were removed by the standard lift-off process. The lift-off process involved four ultrasonic steps in which substrates were sequentially immersed in acetone, isopropanol, AZ 300MIF developer, and deionized water. In this way, batch production of Au-patterned SiO_2 substrates could be achieved. It was noted that SiO_2 etching was necessary before metal deposition to get a flat substrate.

Mechanical Exfoliation: The Au-patterned SiO_2 substrates were cleaned using RIE with argon as the etching gas for 1 min. The freshly cleaved layered crystals on PDMS (Gel-Pak) were then immediately pressed onto the cleaned substrates for ≈20 s on a hotplate heated to 100 °C. After gently separating the substrates and PDMS, large-area 2D atomically thin crystals could be obtained on Au-patterned SiO_2 substrates.

Raman and PL Characterizations: Raman and PL spectroscopies were mainly performed by a WITec alpha 300R confocal Raman microscope. The signals were excited using the 532 nm laser focused by a 100× microscope objective. The laser power was set to 0.5–2 mW for TMDs (WS_2, MoS_2, WSe_2, and $MoSe_2$), 0.1 mW for $NbSe_2$, and 0.5 mW for BP. Raman spectra of $Cr_2Ge_2Te_6$ were performed by a Horiba HR Evolution confocal Raman microscope with a laser power of 0.2 mW. During optical characterizations, $NbSe_2$, BP, and $Cr_2Ge_2Te_6$ thin layers were protected by PMMA capping layers.

Fabrication Process of Transport Devices: The BP, $NbSe_2$, and MoS_2 layers on exposed rectangular SiO_2 substrates were exfoliated using the Au-template-assisted mechanical exfoliation method. Thin hBN flakes (10–20 nm) were deposited onto the exfoliated atomic flakes with rectangular shapes by the deterministic transfer method.[20] A poly(propylene) carbonate (PPC) film was placed on a hemispherical polydimethylsiloxane (PDMS) to create the PPC/PDMS stamp mounted on a glass slide. The stamps were used to pick up the hBN-capped atomic layers to form BP ($NbSe_2$ or MoS_2)/hBN/PPC/PDMS stacks at ≈45 °C. For top-gated BP FETs, the stacks were slowly deposited onto pre-patterned Cr/Au (3 nm/18 nm) serving as the source and drain electrodes at 80–90 °C. At this temperature, the viscosity of PPC was decreased, allowing it to be detached from hBN. Then, the exfoliated graphite flakes on PDMS were transferred onto hBN to serve as top-gate electrodes. For $NbSe_2$ Hall devices, the stacks were carefully deposited onto pre-patterned Cr/Au (3 nm/18 nm) Hall bar electrodes. For top-gated MoS_2 FETs, the stacks were slowly released onto two closely spaced (5–10 µm) graphite flakes serving as the source and drain electrodes. Then, Cr/Au (5 nm/50 nm) top-gate electrodes were defined by standard electron-beam lithography and deposited by EBD.

Transport Measurements: Electrical characterizations of top-gated MoS_2 (monolayer, bilayer, and tri-layer) and BP (bilayer, four-layer, and six-layer) FETs were carried out using a Keithley 4200 semiconductor characterization system (4200-SCS) and a Janis probe station at a vacuum of 10^{-5} Torr. Transport measurements of bilayer, trilayer $NbSe_2$ Hall devices were performed in a He-3 cryostat with a superconducting magnet (HelioxVT, Oxford Instruments). The longitudinal resistance was measured by a four-probe method with an AC probe current $I_{ac} = 1$ µA. Transport measurements of five-layer and bulk $NbSe_2$ Hall devices were performed in a Physical Property Measurement System (PPMS, Quantum Design Inc.) using the resistivity option with an AC drive mode.

Construction of Moiré Superlattice: 1) Twisted MoS_2 homobilayers were fabricated using hBN/PPC/PDMS stamps mounted on glass slides to sequentially pick up two adjacent monolayer MoS_2 flakes at a certain twist angle (see Figure S13, Supporting Information). The PPC film together with the stacked sample was then peeled, flipped over, and placed onto a Si/SiO_2 (285 nm) substrate for subsequent AFM characterizations. 2) Twisted WS_2/WSe_2 heterobilayers were fabricated by angle-aligning the straight steps across crystal layers. First, two adjacent WS_2 flakes and two adjacent WSe_2 flakes on rectangular SiO_2 substrates with specific crystal orientations determined by their nearby straight steps (Figure S17, Supporting Information) were selected, and transferred thin hBN flakes onto WSe_2 flakes. Second, PPC/PDMS stamps were used to pick up one WSe_2/hBN stack at 45 °C and angle-aligned the WSe_2 flake with one WS_2 flake through their nearby straight steps across crystal layers. Third, the WSe_2/hBN stack on the PPC/PDMS stamp was slowly released onto the WS_2 flake at 80 °C. The fabrication process allowed the simultaneous creation of both R-stacking (0°) and H-stacking (60°) twisted WS_2/WSe_2 heterolayers (Figure S18, Supporting Information). 3) Fabrication processes for twisted multilayer-MoS_2 homojunctions were similar to those for twisted MoS_2 homobilayers.

AFM Characterization: AFM imaging was performed with an Asylum Research Cypher S AFM. Lateral Force Microscopy (LFM) for atomic-resolution images was conducted using a conductive Au-coated tip (NANOSENSOR qp-BioAC). Vector PFM and DART (dual AC resonance tracking) PFM for visualization of moiré patterns were carried out using a conductive diamond-coated tip (Adama AD-2.8-AS).

Second-Harmonic-Generation Characterization: The polarization-resolved SHG measurements and SHG imaging were performed on a WITec alpha 300RA confocal Raman microscope (see Figure S19, Supporting Information), using a 1064-nm laser generated by an NPI Rainbow picosecond-laser system (pulse width ≈15 ps, repetition rate of 80 MHz). The laser power was adjusted from 4 to 20 mW. A half-wave plate was set in the common optical path of the incident laser and the SHG signal. It was utilized to control the polarization direction of the incident laser automatically by software. To facilitate the determination of the armchair and zigzag directions of monolayer TMDs, a laboratory coordinate system was established with *x*, *y*, and *z*-axes. The initial laser polarization and the initial fast axis of the half-wave plate were along the *x*-axis. During the polarization-resolved SHG measurements, the half-wave plate was rotated clockwise in the *xy* plane. The SHG signal was first spectrally filtered, and then decomposed parallel (*x*) or perpendicular (*y*) to the initial laser polarization by an analyzer and finally detected by a UHTS spectrometer system coupled with a CCD detector.

Supporting Information

Supporting Information is available from the Wiley Online Library or from the author.

Acknowledgements

The authors thank X. Xu and H. Liu for helpful discussions. The authors thank W. Wu and S. Ding for the assistance with SHG measurements and R. Zhu for the assistance with the visualization of moiré patterns. This work was supported by the National Key Research & Development Projects of China (grant No. 2022YFA1204100), National Natural Science Foundation of China (grant No. 61888102), Strategic Priority Research Program of Chinese Academy of Sciences (CAS, grant No. XDB30000000 and XDB28000000), Youth Innovation Promotion Association of CAS (Y201902), and CAS Project for Young Scientists in Basic Research (YSBR-003), Beijing Natural Science Foundation (grant No. JQ21002). Work at Vanderbilt University was supported by the McMinn Endowment.

Conflict of Interest

The authors declare no conflict of interest.

Author Contributions

L.B. and H.-J.G. supervised the overall research. K.W., L.B., and H.-J.G. designed the experiments. K.W. exfoliated the materials, performed the optical characterizations, and fabricated the transport devices and moiré superlattices. K.W., H.W., Z.S., and B.F. performed the AFM characterizations. K.W., M.Y., L.L., Z.C., and L.B. carried out the transport measurements. G.H., Y.S., X.H., J.G., and Y.S. provided high-quality crystals. K.W., H.W., K.W., Y.H., Z.C., L.B., S.T.P., and H.-J.G. analyzed the data. K.W., M.Y., B.F., H.Y., L.B., S.T.P., and H.-J.G. wrote the paper. All the authors contributed to the preparation of the manuscript.

Data Availability Statement

The data that support the findings of this study are available from the corresponding author upon reasonable request.

Keywords

2D materials, Au-template-assisted mechanical exfoliation, dry-transfer techniques, interlayer excitons, moiré superlattices

Received: December 11, 2023
Revised: April 7, 2024
Published online:

[1] D. Huang, J. Choi, C.-K. Shih, X. Li, *Nat. Nanotechnol.* **2022**, *17*, 227.
[2] K. F. Mak, J. Shan, *Nat. Nanotechnol.* **2022**, *17*, 686.
[3] T. Li, S. Jiang, B. Shen, Y. Zhang, L. Li, Z. Tao, T. Devakul, K. Watanabe, T. Taniguchi, L. Fu, J. Shan, K. F. Mak, *Nature* **2021**, *600*, 641.
[4] L. J. McGilly, A. Kerelsky, N. R. Finney, K. Shapovalov, E.-M. Shih, A. Ghiotto, Y. Zeng, S. L. Moore, W. Wu, Y. Bai, K. Watanabe, T. Taniguchi, M. Stengel, L. Zhou, J. Hone, X. Zhu, D. N. Basov, C. Dean, C. E. Dreyer, A. N. Pasupathy, *Nat. Nanotechnol.* **2020**, *15*, 580.
[5] Y. Cao, V. Fatemi, S. Fang, K. Watanabe, T. Taniguchi, E. Kaxiras, P. Jarillo-Herrero, *Nature* **2018**, *556*, 43.
[6] G. Chen, A. L. Sharpe, P. Gallagher, I. T. Rosen, E. J. Fox, L. Jiang, B. Lyu, H. Li, K. Watanabe, T. Taniguchi, J. Jung, Z. Shi, D. Goldhaber-Gordon, Y. Zhang, F. Wang, *Nature* **2019**, *572*, 215.
[7] Y. Cao, V. Fatemi, A. Demir, S. Fang, S. L. Tomarken, J. Y. Luo, J. D. Sanchez-Yamagishi, K. Watanabe, T. Taniguchi, E. Kaxiras, R. C. Ashoori, P. Jarillo-Herrero, *Nature* **2018**, *556*, 80.
[8] X. Liu, Z. Hao, E. Khalaf, J. Y. Lee, Y. Ronen, H. Yoo, D. Haei Najafabadi, K. Watanabe, T. Taniguchi, A. Vishwanath, P. Kim, *Nature* **2020**, *583*, 221.
[9] K. Tran, G. Moody, F. Wu, X. Lu, J. Choi, K. Kim, A. Rai, D. A. Sanchez, J. Quan, A. Singh, J. Embley, A. Zepeda, M. Campbell, T. Autry, T. Taniguchi, K. Watanabe, N. Lu, S. K. Banerjee, K. L. Silverman, S. Kim, E. Tutuc, L. Yang, A. H. MacDonald, X. Li, *Nature* **2019**, *567*, 71.
[10] K. L. Seyler, P. Rivera, H. Yu, N. P. Wilson, E. L. Ray, D. G. Mandrus, J. Yan, W. Yao, X. Xu, *Nature* **2019**, *567*, 66.
[11] C. Jin, E. C. Regan, A. Yan, M. Iqbal Bakti Utama, D. Wang, S. Zhao, Y. Qin, S. Yang, Z. Zheng, S. Shi, K. Watanabe, T. Taniguchi, S. Tongay, A. Zettl, F. Wang, *Nature* **2019**, *567*, 76.
[12] E. M. Alexeev, D. A. Ruiz-Tijerina, M. Danovich, M. J. Hamer, D. J. Terry, P. K. Nayak, S. Ahn, S. Pak, J. Lee, J. I. Sohn, M. R. Molas, M. Koperski, K. Watanabe, T. Taniguchi, K. S. Novoselov, R. V. Gorbachev, H. S. Shin, V. I. Fal'ko, A. I. Tartakovskii, *Nature* **2019**, *567*, 81.
[13] H. Park, J. Cai, E. Anderson, Y. Zhang, J. Zhu, X. Liu, C. Wang, W. Holtzmann, C. Hu, Z. Liu, T. Taniguchi, K. Watanabe, J.-h. Chu, T. Cao, L. Fu, W. Yao, C.-Z. Chang, D. Cobden, D. Xiao, X. Xu, *Nature* **2023**, *622*, 74.
[14] A. Weston, E. G. Castanon, V. Enaldiev, F. Ferreira, S. Bhattacharjee, S. Xu, H. Corte-León, Z. Wu, N. Clark, A. Summerfield, T. Hashimoto, Y. Gao, W. Wang, M. Hamer, H. Read, L. Fumagalli, A. V. Kretinin, S. J. Haigh, O. Kazakova, A. K. Geim, V. I. Fal'ko, R. Gorbachev, *Nat. Nanotechnol.* **2022**, *17*, 390.
[15] X. Wang, K. Yasuda, Y. Zhang, S. Liu, K. Watanabe, T. Taniguchi, J. Hone, L. Fu, P. Jarillo-Herrero, *Nat. Nanotechnol.* **2022**, *17*, 367.
[16] C. N. Lau, M. W. Bockrath, K. F. Mak, F. Zhang, *Nature* **2022**, *602*, 41.
[17] S. Carr, S. Fang, E. Kaxiras, *Nat. Rev. Mater.* **2020**, *5*, 748.
[18] K. S. Novoselov, A. K. Geim, S. V. Morozov, D. Jiang, Y. Zhang, S. V. Dubonos, I. V. Grigorieva, A. A. Firsov, *Science* **2004**, *306*, 666.
[19] K. Kim, M. Yankowitz, B. Fallahazad, S. Kang, H. C. P. Movva, S. Huang, S. Larentis, C. M. Corbet, T. Taniguchi, K. Watanabe, S. K. Banerjee, B. J. LeRoy, E. Tutuc, *Nano Lett.* **2016**, *16*, 1989.
[20] A. Castellanos-Gomez, M. Buscema, R. Molenaar, V. Singh, L. Janssen, H. S. J. van der Zant, G. A. Steele, *2D Mater.* **2014**, *1*, 011002.
[21] L. A. Ponomarenko, R. V. Gorbachev, G. L. Yu, D. C. Elias, R. Jalil, A. A. Patel, A. Mishchenko, A. S. Mayorov, C. R. Woods, J. R. Wallbank, M. Mucha-Kruczynski, B. A. Piot, M. Potemski, I. V. Grigorieva, K. S. Novoselov, F. Guinea, V. I. Fal'ko, A. K. Geim, *Nature* **2013**, *497*, 594.
[22] Z. Zheng, Q. Ma, Z. Bi, S. de la Barrera, M.-H. Liu, N. Mao, Y. Zhang, N. Kiper, K. Watanabe, T. Taniguchi, J. Kong, W. A. Tisdale, R. Ashoori, N. Gedik, L. Fu, S.-Y. Xu, P. Jarillo-Herrero, *Nature* **2020**, *588*, 71.
[23] Y. Huang, Y.-H. Pan, R. Yang, L.-H. Bao, L. Meng, H.-L. Luo, Y.-Q. Cai, G.-D. Liu, W.-J. Zhao, Z. Zhou, L.-M. Wu, Z.-L. Zhu, M. Huang, L.-W. Liu, L. Liu, P. Cheng, K.-H. Wu, S.-B. Tian, C.-Z. Gu, Y.-G. Shi, Y.-F. Guo, Z. G. Cheng, J.-P. Hu, L. Zhao, G.-H. Yang, E. Sutter, P. Sutter, Y.-L. Wang, W. Ji, X.-J. Zhou, et al., *Nat. Commun.* **2020**, *11*, 2453.
[24] M. Velický, G. E. Donnelly, W. R. Hendren, S. McFarland, D. Scullion, W. J. I. DeBenedetti, G. C. Correa, Y. Han, A. J. Wain, M. A. Hines, D. A. Muller, K. S. Novoselov, H. D. Abruña, R. M. Bowman, E. J. G. Santos, F. Huang, *ACS Nano* **2018**, *12*, 10463.
[25] F. Liu, W. Wu, Y. Bai, S. H. Chae, Q. Li, J. Wang, J. Hone, X. Y. Zhu, *Science* **2020**, *367*, 903.
[26] Y. Deng, Y. Yu, Y. Song, J. Zhang, N. Z. Wang, Z. Sun, Y. Yi, Y. Z. Wu, S. Wu, J. Zhu, J. Wang, X. H. Chen, Y. Zhang, *Nature* **2018**, *563*, 94.
[27] Z. Sun, X. Han, Z. Cai, S. Yue, D. Geng, D. Rong, L. Zhao, Y.-Q. Zhang, P. Cheng, L. Chen, X. Zhou, Y. Huang, K. Wu, B. Feng, *Sci. Bull.* **2022**, *67*, 1345.
[28] A. Grubišić-Čabo, M. Michiardi, C. E. Sanders, M. Bianchi, D. Curcio, D. Phuyal, M. H. Berntsen, Q. Guo, M. Dendzik, *Adv. Sci.* **2023**, *10*, 2301243.
[29] Y. Huang, Y.-K. Wang, X.-Y. Huang, G.-H. Zhang, X. Han, Y. Yang, Y. Gao, L. Meng, Y. Wang, G.-Z. Geng, L.-W. Liu, L. Zhao, Z.-H. Cheng, X.-F. Liu, Z.-F. Ren, H.-X. Yang, Y. Hao, H.-J. Gao, X.-J. Zhou, W. Ji, Y.-L. Wang, *InfoMat* **2021**, *4*, e12274.
[30] Z. Li, L. Ren, S. Wang, X. Huang, Q. Li, Z. Lu, S. Ding, H. Deng, P. Chen, J. Lin, Y. Hu, L. Liao, Y. Liu, *ACS Nano* **2021**, *15*, 13839.
[31] H. Li, J. Wu, X. Huang, G. Lu, J. Yang, X. Lu, Q. Xiong, H. Zhang, *ACS Nano* **2013**, *7*, 10344.
[32] L. Li, J. Kim, C. Jin, G. J. Ye, D. Y. Qiu, F. H. da Jornada, Z. Shi, L. Chen, Z. Zhang, F. Yang, K. Watanabe, T. Taniguchi, W. Ren, S. G. Louie, X. H. Chen, Y. Zhang, F. Wang, *Nat. Nanotechnol.* **2017**, *12*, 21.
[33] D. Chareev, E. Osadchii, T. Kuzmicheva, J.-Y. Lin, S. Kuzmichev, O. Volkova, A. Vasiliev, *CrystEngComm* **2013**, *15*, 1989.
[34] A. Michail, N. Delikoukos, J. Parthenios, C. Galiotis, K. Papagelis, *Appl. Phys. Lett.* **2016**, *108*, 173102.
[35] U. Bhanu, M. R. Islam, L. Tetard, S. I. Khondaker, *Sci. Rep.* **2014**, *4*, 5575.
[36] M. Velický, A. Rodriguez, M. Bouša, A. V. Krayev, M. Vondráček, J. Honolka, M. Ahmadi, G. E. Donnelly, F. Huang, H. D. Abruña, K. S. Novoselov, O. Frank, *J. Phys. Chem. Lett.* **2020**, *11*, 6112.
[37] C. R. Dean, A. F. Young, I. Meric, C. Lee, L. Wang, S. Sorgenfrei, K. Watanabe, T. Taniguchi, P. Kim, K. L. Shepard, J. Hone, *Nat. Nanotechnol.* **2010**, *5*, 722.
[38] L. Wang, I. Meric, P. Y. Huang, Q. Gao, Y. Gao, H. Tran, T. Taniguchi, K. Watanabe, L. M. Campos, D. A. Muller, J. Guo, P. Kim, J. Hone, K. L. Shepard, C. R. Dean, *Science* **2013**, *342*, 614.
[39] Y. Cao, A. Mishchenko, G. L. Yu, E. Khestanova, A. P. Rooney, E. Prestat, A. V. Kretinin, P. Blake, M. B. Shalom, C. Woods, J. Chapman, G. Balakrishnan, I. V. Grigorieva, K. S. Novoselov, B. A. Piot, M. Potemski, K. Watanabe, T. Taniguchi, S. J. Haigh, A. K. Geim, R. V. Gorbachev, *Nano Lett.* **2015**, *15*, 4914.
[40] X. Wang, J.-B. Xu, W. Xie, J. Du, *J. Phys. Chem. C* **2011**, *115*, 7596.
[41] X. Wang, J.-B. Xu, C. Wang, J. Du, W. Xie, *Adv. Mater.* **2011**, *23*, 2464.
[42] X. Xi, Z. Wang, W. Zhao, J.-H. Park, K. T. Law, H. Berger, L. Forró, J. Shan, K. F. Mak, *Nat. Phys.* **2016**, *12*, 139.
[43] L. Li, Y. Yu, G. J. Ye, Q. Ge, X. Ou, H. Wu, D. Feng, X. H. Chen, Y. Zhang, *Nat. Nanotechnol.* **2014**, *9*, 372.

[44] D. J. Perello, S. H. Chae, S. Song, Y. H. Lee, *Nat. Commun.* **2015**, *6*, 7809.
[45] X. Wang, A. M. Jones, K. L. Seyler, V. Tran, Y. Jia, H. Zhao, H. Wang, L. Yang, X. Xu, F. Xia, *Nat. Nanotechnol.* **2015**, *10*, 517.
[46] A. W. Tsen, B. Hunt, Y. D. Kim, Z. J. Yuan, S. Jia, R. J. Cava, J. Hone, P. Kim, C. R. Dean, A. N. Pasupathy, *Nat. Phys.* **2016**, *12*, 208.
[47] L. M. Malard, T. V. Alencar, A. P. M. Barboza, K. F. Mak, A. M. de Paula, *Phys. Rev. B* **2013**, *87*, 201401.
[48] N. Kumar, S. Najmaei, Q. Cui, F. Ceballos, P. M. Ajayan, J. Lou, H. Zhao, *Phys. Rev. B* **2013**, *87*, 161403.
[49] J. Kunstmann, F. Mooshammer, P. Nagler, A. Chaves, F. Stein, N. Paradiso, G. Plechinger, C. Strunk, C. Schüller, G. Seifert, D. R. Reichman, T. Korn, *Nat. Phys.* **2018**, *14*, 801.
[50] P. Rivera, K. L. Seyler, H. Yu, J. R. Schaibley, J. Yan, D. G. Mandrus, W. Yao, X. Xu, *Science* **2016**, *351*, 688.
[51] C. Jin, Z. Tao, T. Li, Y. Xu, Y. Tang, J. Zhu, S. Liu, K. Watanabe, T. Taniguchi, J. C. Hone, L. Fu, J. Shan, K. F. Mak, *Nat. Mater.* **2021**, *20*, 940.
[52] Z. Chu, E. C. Regan, X. Ma, D. Wang, Z. Xu, M. I. B. Utama, K. Yumigeta, M. Blei, K. Watanabe, T. Taniguchi, S. Tongay, F. Wang, K. Lai, *Phys. Rev. Lett.* **2020**, *125*, 186803.